JBO Journal of Biomedical Optics

RESEARCH PAPER

Rapid inverse radiative transfer solver for multiparameter spectrophotometry without integrating sphere

Jiahong Jin,[a,b,c] Zachary D. Jones,[b] Jun Q. Lu,[a,b] and Xin-Hua Hu[a,b,*]

[a]Hunan Institute of Science and Technology, Institute for Advanced Optics, Yueyang, China
[b]East Carolina University, Department of Physics, Greenville, North Carolina, United States
[c]Hunan Institute of Science and Technology, School of Physics and Electronic Science, Yueyang, China

ABSTRACT. **Significance:** Multiparameter spectrophotometry (MPS) provides a powerful tool for accurate characterization of turbid materials in applications such as analysis of material compositions, assay of biological tissues for clinical diagnosis and food safety monitoring.

Aim: This work is aimed at development and validation of a rapid inverse solver based on a particle swarm optimization (PSO) algorithm to retrieve the radiative transfer (RT) parameters of absorption coefficient, scattering coefficient and anisotropy factor of a turbid sample.

Approach: Monte Carlo (MC) simulations were performed to obtain calculated signals for comparison to the measured ones of diffuse reflectance, diffuse transmittance and forward transmittance. An objective function has been derived and combined with the PSO algorithm to iterate MC simulations for MPS.

Results: We have shown that the objective function can significantly reduce the variance in calculated signals by local averaging of an inverse squared error sum function between measured and calculated signals in RT parameter space. For validation of the new objective function for PSO based inverse solver, the RT parameters of 20% Intralipid solutions have been determined from 520 to 1000 nm which took about 2.7 minutes on average to complete signal measurement and inverse calculation per wavelength.

Conclusion: The rapid solver enables MPS to be translated into easy-to-use and cost-effective instruments without integrating sphere for material characterization by separating and revealing compositional profiles at the molecular and particulate scales.

Keywords: inverse scattering problems; Monte Carlo modeling; light scattering and absorption; turbid materials; spectrophotometry

Paper 230238SSR received Aug. 24, 2023; revised Nov. 3, 2023; accepted Nov. 28, 2023; published Jan. 2, 2024.

1 Introduction

Conventional spectrophotometers are probably the most commonly used type of instruments for material analysis by determination of absorbance A or attenuation coefficient μ_t as a function of wavelength λ for a given sample. For turbid materials including biological tissues, additional optical parameters are needed to characterize molecular composition and particle sizes on scales

*Address all correspondence to Xin-Hua Hu, hux@ecu.edu

close to λ by their ability to absorb and scatter light. One paradigm is to retrieve these parameters by the radiative transfer (RT) theory,[1] and its spectroscopic implementation is termed multiparameter spectrophotometry (MPS). The RT theory quantifies light–matter interaction by the parameters of absorption coefficient μ_a and scattering coefficient μ_s in addition to a single-scattering phase function $p(\theta, \phi)$ with θ and ϕ as the polar and azimuthal scattering angles. MPS thus requires measurement of multiple light scattering signals to solve multiple inverse scattering problems (ISPs) at selected values of λ that remains challenging for highly turbid samples. To reduce complexity, $p(\theta, \phi)$ of an unknown sample is often modeled by an analytical function of $p_{HG}(\cos\theta)$ proposed by Heyney and Greenstein under the assumption of axially symmetric scattering.[1–3] Alternative model functions have been studied for $p(\theta, \phi)$ but $p_{HG}(\cos\theta)$ is the preferred one with a form fully specified by an anisotropy factor g as the mean value of $\cos\theta$. By choosing p_{HG} as the phase function, MPS is to measure multiple light scattering signals and determine inversely the RT parameters as function of at λ. These parameters can be expressed as a vector of $\mathbf{P}(\lambda) = (\mu_a, \mu_s, g)$.

A widely used approach of MPS is to measure three signals of collimated transmittance T_c, hemispherically integrated diffuse reflectance R_{dh} and transmittance T_{dh} with one or two integrating sphere.[3–11] If only one integrating sphere is used, signals need to be measured in two steps with one for R_{dh} and another one for T_{dh} with T_c acquired in either step. To solve the ISPs, one first derives $\mu_t\ (= \mu_a + \mu_s)$ from T_c by the Beer-Lambert law followed with retrieval of μ_s and g from R_{dh} and T_{dh} using different methods of forward modeling guided by gradient descent based inverse solver. The modeling methods include numerically solving the RT boundary-value problem, adding-doubling algorithm or Monte Carlo (MC) simulations. Despite its popularity as a research tool, the need for two integrating spheres or two steps of signal measurement makes it difficult to translate this approach into an easy-to-use instrument like a conventional spectrophotometer. In addition, the use of integrating sphere limits severely the accessibility of the approach to non-specialists due to time-consuming sample assembly and system maintenance. Other approaches without integrating sphere have been investigated such as goniometric measurement and detection of T_c and non-hemispherical R_d and T_d at fixed angles with MC based inverse algorithms.[12,13]

We have previously shown that the RT parameter vector $\mathbf{P}$ can be uniquely determined from three simultaneously measured signals of non-hemispherical diffuse reflectance R_d, diffuse transmittance T_d and forward transmittance T_f without integrating sphere.[14,15] MC simulations are performed to accurately calculate signals as R_{dc}, T_{dc}, and T_{fc} and repeated to match the measured ones. A gradient descent algorithm has been developed to guide iteration in the RT parameter space to minimize an objective function $\delta(\mathbf{P})$ defined as the sum of squared percentage differences between the measured and calculated signals. An ISP at λ is deemed as solved with $\mathbf{P}_s$ when $\delta(\mathbf{P}_s) \leq \delta_{th}$ in which δ_{th} represents a threshold based on the experimental errors in signal measurement. The inherent statistical variance in the calculated signals, however, makes it difficult to accurately solve ISPs for highly turbid and optically thick samples by gradient decent despite the existence of a unique solution.[16] Specifically, sizable regions of small δ values exist in the RT parameter space of $\mathbf{P}$ for these ISPs of large scattering albedo $a(= \mu_s/\mu_t)$ and optical thickness $\tau(= \mu_t D)$ with D as sample thickness. In such regions, values of $\delta(\mathbf{P})$ fluctuate considerably due to the variance of MC simulations that often lead to errors in the solution given by $\mathbf{P}_s$. To solve these challenging ISPs for highly turbid samples, one needs to either significantly increase the number of photons in MC simulations for variance reduction or search manually by contour analysis of $\delta(\mathbf{P})$ distributions in the RT parameter space. Either way gives rise to high computational cost and prevents rapidly solving ISPs for MPS.[16] In this report, we present a rapid inverse solver for MPS based on a particle swarm optimization (PSO) algorithm with a novel objective function $\rho_{1/\delta}(\mathbf{P})$ through local averaging in the space of $\mathbf{P}$ to determine $\mathbf{P}_s(\lambda)$.[17] The function $\rho_{1/\delta}(\mathbf{P})$ significantly reduces the effect of MC simulation variance in calculated signals on inverse calculation by PSO and computation time to solve ISPs by reducing the number of photons in MC simulations. Our validation results with 20% intralipid samples demonstrate that $\mathbf{P}_s(\lambda)$ can be retrieved rapidly between 520 and 1000 nm by executing MC simulations on one GPU board.

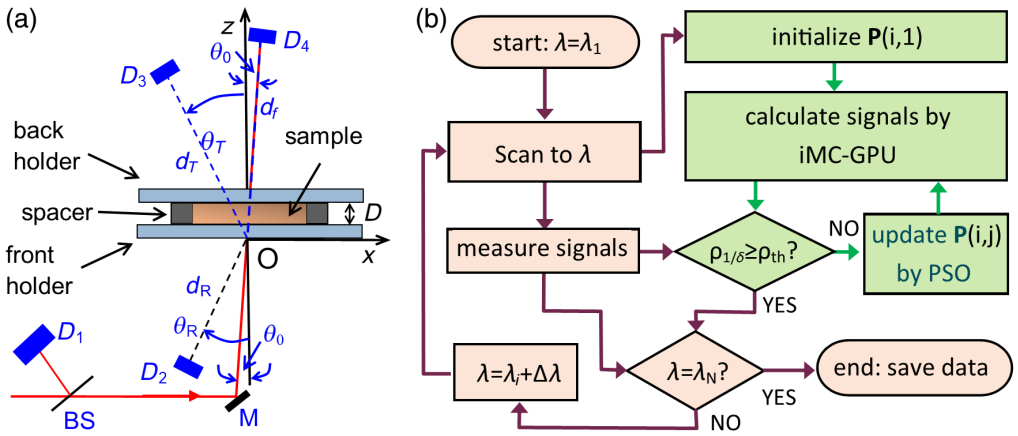

Fig. 1 (a) Configuration of signal detection with incident beam indicated by the red line: D: sample thickness; D_1: for monitoring I_0; M: mirror; D_2 to D_4: for measurement of I_{Rd}, I_{Td}, and I_{Tf}; θ_0: angle of incident beam from z-axis; d_R, d_T, and d_f: distance between the origin and front center of D_2, D_3, and D_4; and θ_R, θ_T, and θ_f: angle of sensor surface normal (blue dash lines) of D_2, D_3, and D_4 from the z-axis. (b) Work-flow chart of signal measurement in brown boxes and inverse calculation in green boxes.

2 Materials and Methods

2.1 Signal Measurement by MPS

An experimental system has been constructed to measure $R_d(\lambda)$, $T_d(\lambda)$, and $T_f(\lambda)$ for validation of the new inverse solver with the signal detection configuration shown in Fig. 1(a). The details of the experimental system were previously reported.[18] Briefly, a xenon light source (XL1-175-A, WavMed Technologies Corp.) and a monochromator (CM110, CVI Corp.) are employed to produce a monochromatic beam with λ adjustable between 520 and 1000 nm in steps of 20 nm and bandwidths around 5 nm. The beam is modulated at a frequency of $f_0 = 370$ Hz by a mechanical chopper (SR540, Stanford Research Systems) and incident on an assembly consisting of a turbid sample confined in a spacer ring between two glass slides. The intensity of the incident beam I_0 is monitored by a photodiode of D_1 (FDS1010, Thorlabs, Inc.). Three photodiodes (FDS100, Thorlabs, Inc.) of D_2 to D_4 are used to measure respectively I_{Rd} for diffusely reflected, I_{Td} for diffusely transmitted and I_{Tf} for forwardly transmitted light intensity. The current signals of photodiodes were amplified by an in-house built four-channel lock-in amplifier to obtain the measured signals of $R_d = I_{\mathrm{Rd}}/I_0$, $T_d = I_{\mathrm{Td}}/I_0$ and $T_f = I_{Tf}/I_0$. Figure 1(a) shows the detection configuration for acquisition of measured signals from the sample assembly.

2.2 Signal Calculation by iMC

An in-house developed individual photon tracking MC (iMC) code was employed to calculate signals as R_{dc}, T_{dc} and T_{fc} from given $\mathbf{P}$ for a phantom of the same shape as the sample inside a spacer between two glass slides by tracking N_0 photons, which imports the parameters of sample size and detection configuration as input data.[16,19,20] The code injects each of the N_0 photons incident on the sample assembly and then tracks the photon once it transports inside a glass slide or sample until it is either absorbed inside the sample or escapes into air. The exit location and propagation direction of an escaping photon on a glass slide surface are used to determine if it hits a detector for detection. A counter associated with each detector records the number of detected photons as N_{Rd}, N_{Td}, and N_{Tf} by the detector D_2, D_3, and D_4, respectively. The above process repeats until the total number of injected photons reaches N_0 and the calculated signals are given by $R_{\mathrm{dc}} = N_{\mathrm{Rd}}/N_0$, $T_{\mathrm{dc}} = N_{\mathrm{Rd}}/N_0$ and $T_{\mathrm{fc}} = N_{\mathrm{Tf}}/N_0$. Because of independence in trajectory among the N_0 photons, the numbers of detected photons follow Poisson distributions.[21] To estimate the variance in these photon numbers, one can draw a random number q of Poisson distribution with $f(q, q_m)$ as probability mass function and q_m as the mean. In the case of N_{Rd} calculated by an iMC simulation, q_m equals to $N_0 R_{\mathrm{dc}\infty}$ if distribution of N_{Rd} follows $f(N_{\mathrm{Rd}}, q_m)$ and $R_{\mathrm{dc}\infty}$ yields the variance-free value of R_{dc} by tracking "infinite" number of photons. One thus can use $f(q, q_m)$ to quantify the effect of variance on calculated signals and optimize the objective function for variance reduction.

2.3 PSO Algorithm

A stochastic algorithm based on PSO has been developed to guide iMC simulations and solve for $\mathbf{P}_s(\lambda)$ in the RT parameter space from measured signals by optimizing an objective function as shown in Fig. 1(b). An objective function quantifies the difference between measured signals and calculated ones obtained by given $\mathbf{P}(\lambda)$, and optimization of this function reduces the difference to solve for $\mathbf{P}_s(\lambda)$ from an initial choice of $\mathbf{P}(\lambda)$. The PSO algorithm was chosen for its high efficiency and ability to perform global search or avoid local traps in the RT parameter space. A search proceeds through multiple threads in PSO, and the threads are represented by a swarm of "particles" with index i $\in [1, \mathrm{I}]$ and I as the number of threads or particles. Here, a particle i symbolizes a thread of positions in the RT parameter space along which it moves from $\mathbf{P}(i,j)$ to $\mathbf{P}(i,j+1)$ as[22]

$$\begin{aligned}\mathbf{P}(i,j+1) &= \mathbf{P}(i,j) + \mathbf{v}(i,j+1),\\ \mathbf{v}(i,j+1) &= \chi\{w_0\mathbf{v}(i,j) + w_p q(\mathbf{P}_p(i) - \mathbf{P}(i,j)) + w_g q\prime(\mathbf{P}_g - \mathbf{P}(i,j))\},\end{aligned} \tag{1}$$

where $j \in [1, J]$; J is the number of iterations; $\mathbf{v}$ is the particle's velocity; q and q' are random numbers of uniform distribution from 0 to 1; $\mathbf{P}_p(i)$ is the particle-best position; $\mathbf{P}_g$ is the swarm-best position; w_0, w_p, and w_g are weights of terms contributing to $\mathbf{v}(i, j+1)$; and χ is a damping constant to increase stability. A particle transits toward $\mathbf{P}_p(i)$ and $\mathbf{P}_g$ through completed iterations by Eq. (1) that respectively yields the best position of that particle and all particles for optimized objective function to reduce difference between calculated and measured signals. By setting values of w_p and w_g equal and large in comparison to w_0 in Eq. (1), for example, enables fast convergence of all particles from their best positions $\mathbf{P}_p(i)$ towards $\mathbf{P}_g$ on average as j increases. A region Γ_s in the RT parameter space is designated as the search space and $\mathbf{P}(i, j+1)$ in Eq. (1) is set to $\mathbf{P}(i, j)$ if the former moves out of Γ_s. The search stops once the objective function at $\mathbf{P}_g$ reaches a preset threshold or j exceeds J and current $\mathbf{P}_g$ is saved as $\mathbf{P}_s(\lambda)$ for output.

3 Results and Discussion

3.1 Effect of Variance in Calculated Signals on Solving ISPs

MPS requires solving one ISP for each value of λ from the measured signals. The first step is to perform forward calculations of signals from given $\mathbf{P} = (\mu_a, \mu_s, g)$ by iMC simulations of light–matter interaction in the sample. The calculated signals can be normalized by respective measured signals and expressed as a vector of $\mathbf{S_c}(\mathbf{P}) = (R_{\mathrm{dc}}(\mathbf{P})/R_d,\ T_{\mathrm{dc}}(\mathbf{P})/T_d, T_{\mathrm{fc}}(\mathbf{P})/T_f)$. An inverse algorithm is to iterate iMC simulations toward the objective of making $\mathbf{S_c}(\mathbf{P})$ as close to $\mathbf{1} = (1,1,1)$ as possible. A function of squared error sum $\delta(\mathbf{P}) = |\mathbf{S_c}(\mathbf{P}) - \mathbf{1}|^2$ is often selected as the objective function to guide iteration and decide when stops. Ideally, $\delta(\mathbf{P}_s)$ vanishes for a perfect ISP solution given by $\mathbf{P}_s$. In practice, one deems an ISP as solved if $\delta(\mathbf{P}) \le \delta_{th}$ with δ_{th} representing a threshold determined by the error level in signal measurement. To quantify the effect of variance in calculated signals by a stochastic iMC simulation, we define a fluctuation vector for calculated signals as

$$\mathbf{f_c} = \left(\frac{R_{\mathrm{dc}}(\mathbf{P})}{R_{\mathrm{dc}\infty}(\mathbf{P})} - 1, \frac{T_{\mathrm{dc}}(\mathbf{P})}{T_{\mathrm{dc}\infty}(\mathbf{P})} - 1, \frac{T_{\mathrm{fc}}(\mathbf{P})}{T_{\mathrm{fc}\infty}(\mathbf{P})} - 1\right), \tag{2}$$

where $R_{\mathrm{dc}\infty}$, $T_{\mathrm{dc}\infty}$, and $T_{\mathrm{fc}\infty}$ are the variance-free signals calculated by tracking "infinite" numbers of photons. It should be noted that $\mathbf{f}_c$ is independent of $\mathbf{P}$ and one can express $\mathbf{S}_c(\mathbf{P})$ by $\mathbf{f}_c$

$$\mathbf{S}_c(\mathbf{P}) = \left(\frac{R_{\mathrm{dc}}(\mathbf{P})}{R_d}, \frac{T_{\mathrm{dc}}(\mathbf{P})}{T_d}, \frac{T_{\mathrm{fc}}(\mathbf{P})}{T_f}\right) = \mathbf{S}_{c\infty}(\mathbf{P}) + \mathbf{S}_{c\infty}(\mathbf{P}) \circ \mathbf{f_c}, \tag{3}$$

with $\mathbf{S_{c\infty}}(\mathbf{P}) = (R_{\mathrm{dc}\infty}(\mathbf{P})/R_d, T_{\mathrm{dc}\infty}(\mathbf{P})/T_d, T_{\mathrm{fc}\infty}(\mathbf{P})/T_f)$ and "o" denoting the vector form of component-wise product. Combining these results, $\delta(\mathbf{P})$ can now be written as

$$\begin{aligned}\delta(\mathbf{P}) &= \left(\frac{R_{dc}(\mathbf{P})}{R_d} - 1\right)^2 + \left(\frac{T_{dc}(\mathbf{P})}{T_d} - 1\right)^2 + \left(\frac{T_{dc}(\mathbf{P})}{T_d} - 1\right)^2 = \{\mathbf{S}_c(\mathbf{P}) - \mathbf{1}\} \cdot \{\mathbf{S}_c(\mathbf{P}) - \mathbf{1}\}\\ &= \delta_f(\mathbf{P}) + 2\mathbf{f}_c \cdot \{\mathbf{S}_{c\infty}(\mathbf{P}) \circ (\mathbf{S}_{c\infty}(\mathbf{P}) - \mathbf{1})\} + |\mathbf{S}_{c\infty}(\mathbf{P}) \circ \mathbf{f_c}|^2,\end{aligned} \tag{4}$$

where $\delta_f(\mathbf{P}) = |\mathbf{S}_{c\infty}(\mathbf{P}) - \mathbf{1}|^2$ is the variance-free value of $\delta(\mathbf{P})$. It is clear that $\delta_f(\mathbf{P}_s) = 0$ if $\mathbf{P}_s$ represents a "true" solution of ISP.

3.2 Comparison of Two Objective Functions for Variance Suppression

Based on above analysis, local averaging on $\delta(\mathbf{P})$ in the RT parameter space was first employed to suppress variance and hence increase the stability of inverse solutions. We then compared two objective functions defined below on their abilities to further reduce the effect of variance

$$\rho_\delta(\mathbf{P}) = \frac{1}{m_\mathbf{P}} \sum_{\mathbf{P}\prime \in A_\mathbf{P}} \delta(\mathbf{P}\prime), \rho_{1/\delta}(\mathbf{P}) = \frac{1}{m_\mathbf{P}} \sum_{\mathbf{P}\prime \in A_\mathbf{P}} \frac{1}{\delta(\mathbf{P}\prime)}, \tag{5}$$

where $A_\mathbf{P}$ is a set of $m_\mathbf{P}$ vectors consisting of $\mathbf{P}$ and its neighbors on a 3D grid of $\mathbf{P}$. The components of $\mathbf{f}_c$ as defined in Eq. (2) can be obtained as $(q/q_m) - 1$ by drawing a random number q independently from $f(q, q_m)$ and setting the q_m values, related to $R_{dc\infty}, T_{dc\infty}$, and $T_{fc\infty}$, equal to focus on the effect of variance for simplicity. We further set $m_\mathbf{P} = 7$ with $\mathbf{P}$ and its nearest neighbors as the members of $A_\mathbf{P}$ and assumed that all of them have the same value of $\delta_f(\mathbf{P})$. The values of $\rho_\delta(\mathbf{P})$ and $\rho_{1/\delta}(\mathbf{P})$ are plotted in Fig. 2(a) against $\delta_f(\mathbf{P})$ ranging from 0.1% to 1% with a solid line representing $\delta_f(\mathbf{P})$ or $\delta_f(\mathbf{P})^{-1}$. These results show clearly that $\rho_{1/\delta}(\mathbf{P})$ fluctuates significantly less than $\rho_\delta(\mathbf{P})$ for $\delta_f(\mathbf{P})$ between 0.6% and 1%, which is the typical range of δ_{th} set by the error level of measured signals.[16]

To gain further insight on fluctuation in calculated signals, the relative difference Δ between $\rho_\delta(\mathbf{P})$ and $\delta_f(\mathbf{P})$ or $\rho_{1/\delta}(\mathbf{P})$ and $\delta_f(\mathbf{P})^{-1}$ are calculated and averaged as

$$\Delta(\rho_\delta) = \frac{1}{m_\delta} \sum_{\delta_f=0.1\%}^{1.1\%} \left| \frac{\rho_\delta(\mathbf{P}) - \delta_f(\mathbf{P})}{\delta_f(\mathbf{P})} \right|, \tag{6}$$

and

$$\Delta(\rho_{1/\delta}) = \frac{1}{m_\delta} \sum_{\delta_f=0.1\%}^{1.1\%} \left| \frac{\rho_{1/\delta}(\mathbf{P}) - \delta_f(\mathbf{P})^{-1}}{\delta_f(\mathbf{P})^{-1}} \right|, \tag{7}$$

where δ_f is uniformly sampled between 0.1% and 1.1% in each sum and m_δ is the total number of δ_f samples in the sums. The sampled values of $\delta_f(\mathbf{P})$ correspond to the mean values of each signal term in $\delta_f(\mathbf{P})$ ranging from 1.8% to 6.1% since $\delta_f(\mathbf{P})$ is defined as the sum of squared relative differences of calculated and measured values on three signals. Figure 2(b) illustrates the dependence of the two Δ functions on q_m values with m_δ set to 1000. As discussed before, q_m represents the mean value of $f(q, q_m)$ which is the probability mass function of Poisson distribution for modeling detected photon numbers, such as N_{Rd} and related calculated signal

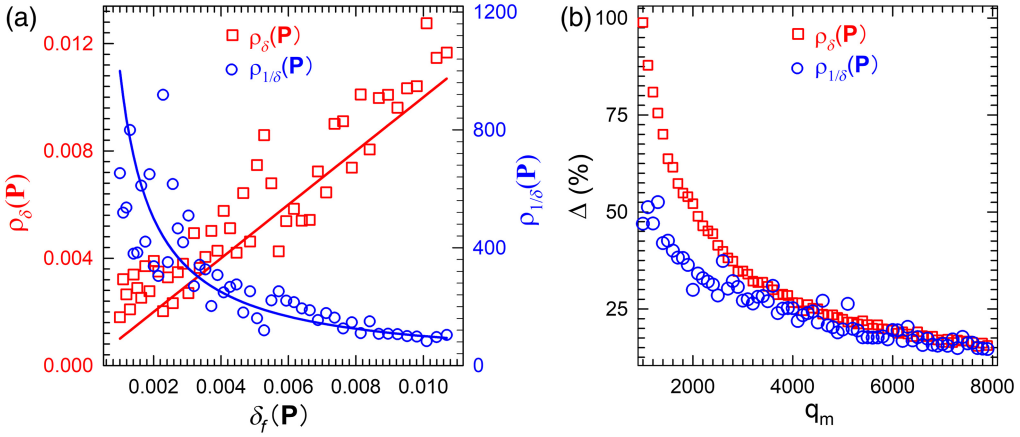

Fig. 2 (a) The dependence of $\rho_\delta(\mathbf{P})$ and $\rho_{1/\delta}(\mathbf{P})$ on $\delta_f(\mathbf{P})$ with red line for $\delta_f(\mathbf{P})$ and blue line for $\delta_f(\mathbf{P})^{-1}$. (b) The mean values of relative differences $\Delta(\rho_\delta)$ between $\rho_\delta(\mathbf{P})$ and $\delta_f(\mathbf{P})$ and $\Delta(\rho_{1/\delta})$ between $\rho_{1/\delta}(\mathbf{P})$ and $\delta_f(\mathbf{P})^{-1}$ against q_m as the mean of Poisson distributions for calculated signals by tracking "infinite" photons.

R_{dc}. Therefore, the ratio of q_m/N_0 equals to $R_{dc\infty}$ as the variance-free value of R_{dc} in the above case and larger q_m corresponds to larger N_0. The results in Fig. 2(b) demonstrate that use of $\rho_{1/\delta}(\mathbf{P})$ instead of $\rho_\delta(\mathbf{P})$ or $\delta(\mathbf{P})$ as the objective function can significantly reduce the variance of calculated signals for the same value of N_0. Alternatively, N_0 can be considerably reduced for the same variance to speed up forward calculations if $\rho_{1/\delta}(\mathbf{P})$ is adopted. For example, computational time of iMC simulations can be cut in half with $\rho_{1/\delta}(\mathbf{P})$, instead of $\rho_\delta(\mathbf{P})$, as the objective function by tracking half of photons with similar variance.

3.3 Measurement of 20% Intralipid Sample

To validate the new approach, RT parameters of 20% intralipid (I141-100ML, Sigma-Aldrich) have been determined from three measured signals of R_d, T_d, and T_f for λ from 520 to 1000 nm in steps of 20 nm. Figure 3 presents the RT parameters of a sample with thickness $D = 102$ μm obtained by the PSO based algorithm with $\rho_{1/\delta}(\mathbf{P})$ selected as the objective function. Signal measurement was repeated three times to obtain the mean values and standard deviations which are plotted in Fig. S1 in the Supplementary Material. Previously determined values of real refractive index $n_r(\lambda)$ of the 20% intralipid were used to obtain interpolated values in iMC simulations at the wavelengths of measurement for the calculated signals and $n_r(\lambda)$ is presented in Fig. S2 in the Supplementary Material.[23] The same measurements were repeated on another sample of $D = 81$ μm and the inversely determined RT parameters agree well with those in Fig. 3 within the experimental errors.

The search region Γ_s for PSO based inverse algorithm at each wavelength was set between 1.00×10^{-4} and 2.00 mm^{-1} for μ_a, 10.0 and 200 mm^{-1} for μ_s, 0.10 and 1.00 for g. In additional to choosing $I = 27$ for the particle number and $J = 100$, we set $w_0 = 0.900$, $w_p = w_g = 2.05$,

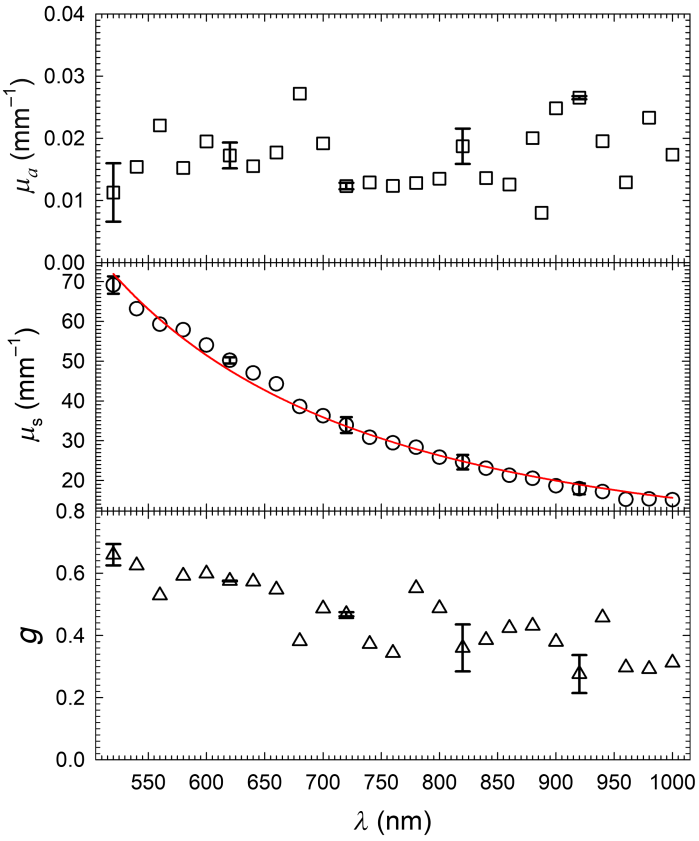

Fig. 3 The wavelength dependence of RT parameters of one 20% intralipid sample of $D = 102$ μm in thickness. The error bars were inversely determined from different combinations of the mean and standard deviation values of the measured signals shown in Fig. S1 in the Supplementary Material on five selected wavelengths. The red line is a power law fitting of $\mu_s = C\lambda^{-2.340}$ with $C = 1.626 \times 10^8$.

and $\chi = 0.730$ for the PSO parameters defined in Eq. (1) for optimized performance of inverse calculations. The initial positions of $\mathbf{P}(i,1)$ for all particles were randomly distributed in each of nine equal partitions of Γ_s to ensure globally optimized solutions of ISPs. We found that the convergence toward the final solution was not affected by the choice of $\mathbf{P}(i,1)$ under the above condition. After calculation of $\rho_{1/\delta}$ with $\mathbf{P}(i,1)$, iterations as defined in Eq. (1) were performed in Γ_s. Specifically, $\mathbf{P}_p(i)$ was set as $\mathbf{P}(i,1)$ for particle i and $\mathbf{P}_g$ as $\mathbf{P}_p(i')$ that has the largest $\rho_{1/\delta}$ value among all particles for $j = 1$ to obtain $\mathbf{v}(i,2)$ and $\mathbf{P}(i,2)$ by Eq. (1). The search then continued as j increases to 2, 3,... and stopped when either $\rho_{1/\delta}(\mathbf{P}_g)$ exceeds ρ_{th} for $j \leq J$ or $j > J$ with $\mathbf{P}_g$ saved as $\mathbf{P}_s(\lambda)$ and output together with $\rho_{1/\delta}(\mathbf{P}_g)$ and $\delta(\mathbf{P}_g)$. The threshold ρ_{th} corresponds to the value of $\rho_{1/\delta}$ in Eq. (5) with δ_{th} set to 0.8% and m_P to 7.

It took about eight iterations on average to solve an ISP of $\mathbf{P}_s(\lambda)$ from the measured signals of 20% intralipid sample. The total numbers of iMC simulations were found to be about 800 for solving each ISP if 27 particles were employed in PSO based search. Signal were calculated by iMC simulations in which N_0 was gradually increased from 5×10^5 to 5×10^6 as δ became 1% or less. On average, over different values of RT parameters and N_0, each iMC simulation took about 0.2 s and solving $\mathbf{P}_s(\lambda)$ per wavelength took about 160 s by executing the code on one GPU board (Nvidia, GeForce RTX 2080 Ti). The results of $\mathbf{P}_s(\lambda)$ in Fig. 3 compare similarly to those obtained by methods using integrating sphere.[8,24] For example, both of the range and wavelength dependence of μ_s and g agree well with those in Ref. 8 for the 20% intralipid sample while the range of μ_a is between those of Ref. 24 for 10% intralipid and Ref. 8. Since the 20% intralipid is high turbid with scattering albedo $a = \mu_s/\mu_t > 98\%$ over the measured wavelengths, the large differences in the values of μ_a can be attributed to the very large errors in determining μ_a with values smaller than μ_s by three orders of magnitude as previously discussed.[8] We note further that the values of optical thickness τ and albedo a of the intralipid sample reach the maximum values of 7.1 and 99.98%, respectively for $\lambda = 520$ nm. Results of our study on samples of 20% intralipid with sufficiently large D values showed that current MPS method with the inverse solver reported here can yield unstable solutions of $\mathbf{P}_s$ when the value of τ becomes larger than 7.1 for very large values of a above 99.9990%. A detailed comparison of the measured and calculated signals and analysis of background noise in signal measurement suggests that the instability of inverse solution is mainly caused by the variance in calculated signals, which may be mitigated without using N_0 much larger than those used for ISPs of $\tau \leq 7.1$ for iMC simulations. A study is underway to further improve the PSO based inverse solver by taking into account the $\delta(\mathbf{P})$ distribution obtained from completed iterations, which is expected to enable accurate measurement of RT parameters for highly turbid samples with τ up to 15 without significant increase of computational cost. Such an improvement can make the approach of MPS concerned here capable of characterizing optically thick samples by their RT parameters for which the conventional approach with integrating sphere fails for inability to accurately measure collimated transmittance T_c.

4 Conclusions

We have analyzed the effect of variance by MC simulations on solving ISPs and proposed a novel objective function to reduce variance in calculated signals and speed up simulations. Combination of the objective function with the PSO algorithm leads to a rapid inverse solver for determination of RT parameters of turbid samples from three measured signals without integrating sphere. The inverse solver has been validated by the results of RT parameter retrieval on samples of 20% intralipid in a wavelength range of 520 to 1000 nm with ISPs solved rapidly using one GPU board. Taken together, we have demonstrated a new approach of MPS, which allows its translation into a powerful and easy-to-use instrument for clear separation and characterization of molecular composition and turbidity.

Disclosures

Authors declare no conflicts of interest.

Code and Data Availability

All data in support of the findings of this paper are available within the article or as supplementary material. Code and other materials associated with this article are available upon request sent to the corresponding author.

Acknowledgments

Authors thank Dr. Kenneth M. Jacobs for help on development of the experimental system. J. Jing acknowledges grant support by Education Department of Hunan Province of China (Grant No. 22B0680).

References

1. H. C. van de Hulst, *Multiple Light Scattering: Tables, Formulas and Applications*, Academic Press, New York (1980).
2. B.-H. Gao et al., "Efficient equation-solving integral equation method based on the radiation distribution factor for calculating radiative transfer in 3D anisotropic scattering medium," *J. Quant. Spectrosc. Radiat. Transf.* **275**, 107886 (2021).
3. S. Y. Jeong et al., "Measurements of scattering and absorption properties of submillimeter bauxite and silica particles," *J. Quant. Spectrosc. Radiat. Transf.* **276**, 107923 (2021).
4. S. A. Prahl, M. J. C. van Gemert, and A. J. Welch, "Determining the optical properties of turbid media by using the adding-doubling method," *Appl. Opt.* **32**(4), 559–568 (1993).
5. L. Wang, S. L. Jacques, and L. Zheng, "MCML-Monte Carlo modeling of light transport in multi-layered tissues," *Comput. Methods Program Biol.* **47**(2), 131–146 (1995).
6. Y. Du et al., "Optical properties of porcine skin dermis between 900 nm and 1500 nm," *Phys. Med. Biol.* **46**(1), 167–181 (2001).
7. X. Ma et al., "Bulk optical parameters of porcine skin dermis tissues at eight wavelengths from 325 to 1557 nm," *Opt. Lett.* **30**(4), 412–414 (2005).
8. C. Chen et al., "A primary method for determination of optical parameters of turbid samples and application to intralipid between 550 and 1630 nm," *Opt. Express* **14**(16), 7420–7435 (2006).
9. P. Lemaillet et al., "Correction of an adding-doubling inversion algorithm for the measurement of the optical parameters of turbid media," *Biomed. Opt. Express* **9**(1), 55–71 (2018).
10. B. W. Xie et al., "Experimental study of the radiative properties of hedgehog-like ZnO–Au composite particles," *J. Quant. Spectrosc. Radiat. Transf.* **232**, 93–103 (2019).
11. F. Bergmann et al., "Precise determination of the optical properties of turbid media using an optimized integrating sphere and advanced Monte Carlo simulations. Part 2: experiments," *Appl. Opt.* **59**(10), 3216–3226 (2020).
12. C. Y. Ma et al., "GPU-accelerated inverse identification of radiative properties of particle suspensions in liquid by the Monte Carlo method," *J. Quant. Spectrosc. Radiat. Transf.* **172**, 146–159 (2016).
13. X. Liang et al., "Spectrophotometric determination of turbid optical parameters without using an integrating sphere," *Appl. Opt.* **55**(8), 2079–2085 (2016).
14. P. Tian et al., "Spectral determination of μa, μs and g from single and multiple scattering signals with one optically thick sample," *J. Quant. Spectrosc. Radiat. Transf.* **245**, 106868 (2020).
15. P. Tian et al., "Multiparameter spectrophotometry platform for turbid sample measurement by robust solutions of radiative transfer problems," *IEEE Trans. Instrum. Meas.* **70**, 6003110 (2021).
16. Y. Qin et al., "Robustness of inverse solutions for radiative transfer parameters from light signals measured with different detection configurations," *J. Quant. Spectrosc. Radiat. Transf.* **274**, 107883 (2021).
17. M. Clerc and J. Kennedy, "The particle swarm - explosion, stability, and convergence in a multidimensional complex space," *IEEE Trans. Evol. Comput.* **6**(1), 58–73 (2002).
18. Z. Jones et al., "Study of inverse solution for multiparameter spectrophotometry by three photodiodes," *Proc. SPIE* **12376**, 1237604 (2023).
19. X. Chen et al., "Fast method for inverse determination of optical parameters from two measured signals," *Opt. Lett.* **38**(12), 2095–2097 (2013).
20. P. Tian et al., "Quantitative characterization of turbidity by radiative transfer based reflectance imaging," *Biomed. Opt. Express* **9**(5), 2081–2094 (2018).
21. G. S. Fishman, *Monte Carlo: Concepts, Algorithms, and Applications*, Springer-Verlag (1996).
22. F. Marini and B. Walczak, "Particle swarm optimization (PSO). A tutorial," *Chemometr. Intell. Lab. Syst.* **149**, 153–165 (2015).
23. H. Ding et al., "Determination of refractive indices of porcine skin tissues and intralipid at eight wavelengths between 325 and 1557 nm," *J. Opt. Soc. Am. A* **22**, 1151–1157 (2005).
24. S. T. Flock et al., "Optical properties of intralipid: a phantom medium for light propagation studies," *Lasers Surg. Med.* **12**(5), 510–519 (1992).

Jiahong Jin received his BS and MS degrees in mathematics and optics from Sun Yat-sen University, China, and his PhD in biomedical physics from East Carolina University, United States. He joined the Physics Faculty, Hunan Institute of Science and Technology (HNIST) in 2014 and the Institute for Advanced Optics of HNIST in 2016. He is conducting research in optical imaging of turbid materials and biological tissues and machine learning study on diffraction image data of cells.

Zachary D. Jones received his BS degree in applied physics from Appalachian State University in the United States and is currently a PhD candidate for the degree in biomedical physics at East Carolina University. He has experience in medical imaging device research and development as a research assistant with Perfusio Corp. His research interests include tissue optics and Monte Carlo modeling of light transport in tissue phantoms.

Jun Q. Lu received her BS and MS degrees in physics from Nankai University, China, in 1983 and 1986, respectively and her PhD in physics from the University of California at Irvine, United States in 1991. She joined the Faculty of Physics, East Carolina University, United States, in 1996. Her research areas included theoretical modeling, numerical simulations, and machine learning-based analysis of light scattering data acquired from biological cells and turbid samples.

Xin-Hua Hu received his BS and MS degrees in physics from Nankai University in China, his MS degree in physics from Indiana University at Bloomington, and his PhD from the University of California at Irvine in 1991. He joined the Physics Faculty of East Carolina University in 1995 and established the Biomedical Laser Laboratory. He conducts and directs research programs in optical imaging and machine learning study of light scattering by cells and in turbid materials including biological tissues.